

Vibrationally mediated dissociation dynamics of H₂O in the $\nu_{\text{OH}}=2$ polyad

Sergey A. Nizkorodov,^{a)} Michael Ziemkiewicz, Tanya L. Myers,^{b)} and David J. Nesbitt^{c)}
JILA, University of Colorado and National Institute of Standards and Technology and Department of Chemistry and Biochemistry, University of Colorado, Boulder, Colorado 80309-0440

(Received 9 June 2003; accepted 18 August 2003)

Vibrationally mediated photodissociation dynamics of jet-cooled H₂O in the $\nu_{\text{OH}}=2$ polyad is studied in a supersonic slit jet expansion. Single rotational states within $|02\rangle^- (\equiv \nu_1 + \nu_3 \text{ in normal mode notation})$, $|02\rangle^+ (\equiv 2\nu_1)$, $|11\rangle^+ (\equiv 2\nu_3)$, and $|01^-2\rangle (\equiv \nu_3 + 2\nu_2)$ vibrational states of H₂O are selectively prepared with near IR overtone pumping, photodissociated at 193 nm, and the resulting nascent internal state distribution of OH fragments probed via laser induced fluorescence. Strong oscillations in rotational, spin-orbit, and lambda-doublet distributions are observed, often in remarkably close agreement with H₂O state-to-state photodissociation studies from both higher and lower ν_{OH} polyads. The influence of initially excited bending and $J_{K_a K_c}$ levels of H₂O on spin-orbit, Λ -doublet, and rotational distributions of OH is examined in detail. Several new dynamical trends are identified, for example, a clear propensity at high N for a strong Λ^+ versus Λ^- inversion in the $\Pi_{3/2}$ spin-orbit manifold, which reverses in the $\Pi_{1/2}$ manifold, suggesting spin-orbit sensitive stereodynamics in the ejection process. Furthermore, the results highlight significant differences in photodissociation dynamics from *gerade* (e.g., $|02\rangle^+$) versus *ungerade* (e.g., $|02\rangle^-$) vibrational states, specifically with respect to OH($v=1$)/OH($v=0$) branching ratios, and signaling a breakdown of the “spectator” model at low vibrational excitation. © 2003 American Institute of Physics. [DOI: 10.1063/1.1616915]

I. INTRODUCTION

Photofragmentation of H₂O in the first absorption band ($A^1B_1 \leftarrow X^1A_1$) has long represented a fundamental paradigm for direct dissociation on a single repulsive potential energy surface (PES).¹ In contrast to photodissociation in the second absorption band ($B^1B_2 \leftarrow X^1A_1$), which involves multiple product channels, conical intersections, and considerable excess internal energy in the OH fragment,² photoinduced bond-breaking via the A^1B_1 state is less complicated, in principle, permitting development of simple physical models of the dissociation event. For example, $A^1B_1 \leftarrow X^1A_1$ excitation produces little change in the HOH bend PES angular anisotropy, which largely accounts for the low degree of rotational angular momentum transferred to the nascent OH product.³ The moderate levels of OH vibrational excitation observed can also be rationalized from a classical perspective by preferred initial motion on the upper potential surface along the symmetric stretch coordinate.^{1,4}

However, when examined on a fully *state-to-state* basis, this rather simple picture for photodissociation of H₂O proves somewhat deceptive, and indeed becomes far richer and dynamically more interesting.^{5–10} The first experiments on photodissociation dynamics of water from single rovibrational excited states were due to Andresen and co-workers.⁶ Their pioneering experiments on state-selected H₂O($J_{K_a K_c}$)

in the $\nu_{\text{OH}}=1$ vibrational polyad revealed surprisingly strong oscillations in the OH fragment quantum state populations as a function of N_{OH} for a single spin-orbit/ Λ -doublet manifold. What made this observation particularly noteworthy was that these same oscillations vanished for photodissociation of rotationally equilibrated water, even when cooled into the lowest two nuclear spin states ($J_{K_a K_c} = 1_{01}, 0_{00}$) at supersonic jet temperatures.¹¹ This oscillatory behavior has since been unambiguously verified in single rovibrational state photodissociation studies of H₂O for higher OH stretching polyads for $\nu_{\text{OH}}=3-5$.^{5,7,9,10} Subsequent experimental and theoretical studies have demonstrated that these oscillations result from coupling between OH angular momentum states in the exit channel. Specifically, a Franck-Condon model projecting the initial HOH wave function into asymptotic OH states was developed by Balintkurti.¹² This has provided an excellent qualitative (and in some test cases, semiquantitative) description of the nascent OH populations,⁸ clearly confirming the extreme sensitivity to the initial rotational and bending states of H₂O. Indeed, this analysis provided the necessary framework to explain how the presence of two $J_{K_a K_c} = 1_{01}, 0_{00}$ nuclear spin isomers in the early beam experiments of Andresen¹¹ had been sufficient to average out all oscillations in the observed OH rotational distributions.

From the perspective of vibrationally mediated control of photofragmentation dynamics, state-selection of H₂O via overtone excitation offers special advantages. As first elucidated by Lawton and Child, the OH stretch structure for H₂O can be best described by polyads, with each polyad containing $\nu_{\text{OH}}+1$ levels corresponding to ν_{OH} quanta distributed

^{a)}Present address: Department of Chemistry, University of California at Irvine, Irvine, CA 92697.

^{b)}Present address: Pacific Northwest National Lab, Richland, WA 99352.

^{c)}Electronic mail: djn@jila.colorado.edu

between the two identical bonds. By virtue of anharmonic detuning effects that increase with v_{OH} , these quantum states can often be quite well described by a single symmetric or antisymmetric linear combination of pure “local mode” excitations (e.g., $|nm\rangle^{\pm} \approx 2^{-1/2}\{|n,m\rangle \pm |m,n\rangle\}$) with perturbative contributions from other nearby members of the same polyad (e.g., $\approx 2^{-1/2}\{|n \pm 1, m \mp 1\rangle \pm |m \mp 1, n \pm 1\rangle\}$). At least for higher polyad numbers ($v_{\text{OH}}=3,4,5$), this has led to the “spectator” paradigm, i.e., a strong propensity for cleavage of the OH bond with greater local mode vibrational excitation, with the surviving OH bond retaining its initial local mode excitation.¹³ For example, elegant experiments in the Crim group demonstrated that 220–250 nm photodissociation of H₂O in $|04\rangle^{-}$ local mode state predominantly results in OH($v=0$) fragments, whereas dissociation of the nearly isoenergetic $|13\rangle^{-}$ state produces mostly OH($v=1$). Indeed, nearly 100% selective bond fission has been demonstrated in analogous HOD studies, for which the OH versus OD stretch local mode behavior is now essentially complete.¹⁴ These studies have been extensively corroborated by exact QM dynamical calculations,¹³ resulting in an impressive level of consensus between theory and experiment.¹ It remains an open question, however, what happens to this spectator paradigm at lower levels of polyad excitation, e.g., where a local mode description of the H₂O stretch vibrations might begin to break down. However, such studies require accessing multiple vibrational states with “tunable” spectator mode character, which do not exist for the lowest $v_{\text{OH}}=0$ and $v_{\text{OH}}=1$ polyads. It therefore proves particularly interesting to explore vibrationally mediated photodissociation in the $v_{\text{OH}}=2$ polyad, which permits access to the lowest OH stretching states (e.g., $|02\rangle^{-}$, $|02\rangle^{+}$, and $|11\rangle^{+}$) with *distinguishable* local mode quanta in the spectator bond.

The thrust of the present work is to explore state-selected photodissociation of H₂O in the $v_{\text{OH}}=2$ polyad, which allows several questions of dynamical interest to be addressed. First of all, as mentioned earlier, such studies can directly access several different intermediate levels, $|02\rangle^{-}$, $|02\rangle^{+}$, and $|11\rangle^{+}$, whereby photodissociation now has the option of either conserving (or destroying) vibrational excitation in the uncleaved OH bond. As a secondary motivation, photolysis of these vibrational states with 193 nm excitation ($E_{\text{total}} \approx 7.3$ eV) samples regions on the upper PES quite energetically similar (see Table I) to those of Crim and co-workers⁷ in the classic $v_{\text{OH}}=4$ studies of H₂O. As a result, one can further explore how photolysis dynamics depend on the initial wave function projection on the upper surface for comparable energies, specifically probing nascent OH product state distributions. Third, as all three of these $v_{\text{OH}}=2$ overtone states are sufficiently bright for vibrationally mediated photofragmentation, the influence of wave function symmetry (*gerade* versus *ungerade*) on the photodissociation dynamics can be directly tested. Finally, as a somewhat more practical consideration, these monomer photodissociation results provide essential background for interpreting vibrationally mediated spectroscopy and dynamics of water containing clusters currently under investigation.¹⁵

The organization of this paper is as follows: Key experimental details relevant to the present work are discussed in

TABLE I. Summary of vibrationally mediated photodissociation dynamics studies of H₂O in the first absorption band ($A^1B_1 \leftarrow X^1A_1$). The H₂O states are labeled using notation $|mn^{\pm}k\rangle$, where m and n are the number of quanta in the OH local mode stretches and k is the number of quanta in the OH local mode bends and k is the number of quanta in the bend (if any). Excess energy refers to the total excitation energy above $D_0(\text{H-OH}) = 5.118$ eV (41 280 cm⁻¹). In some studies, H₂O is excited in Franck–Condon forbidden region, i.e., substantially below the saddle point on the A^1B_1 PES, which is located some 16 000 cm⁻¹ above D_0 . OH populations are normalized to the sum of OH($v=0$) + OH($v=1$).

H ₂ O state	$\lambda_{\text{photolysis}}$ (nm)	E_{excess} (cm ⁻¹)	OH in $v=0$ (%)	OH in $v=1$ (%)	Reference
$ 00\rangle^{+}$	193	10 530	>99.8	<0.2	16
$ 00\rangle^{+}$	157	22 410	50 ^a	50 ^a	11
$ 01\rangle^{-}$	193	14 290	^b		6, 8
$ 01^{-2}\rangle$	193	17 400	^b		This work
$ 02\rangle^{+}$	193	17 730	63(3)	37(3)	This work
$ 02\rangle^{-}$	193	17 780	97.8(3)	2.2(3)	This work
$ 11\rangle^{+}$	193	17 980	47(5)	53(5)	This work
$ 03\rangle^{+}$	248	9 640	^b		10
$ 03\rangle^{-}$	248	9 660	>99.5	<0.5	10
$ 12\rangle^{+}$	248	9 910	^b		10
$ 12\rangle^{-}$	248	10 070	>98	<2	10
$ 03^{-1}\rangle$	218.5	16 640	>90	<10	9
$ 03^{-2}\rangle$	218.5	18 140	>90	<10	9
$ 04\rangle^{-}$	282	8 010	^b		5
$ 04\rangle^{-}$	266	10 140	>98	<2	7
$ 04\rangle^{-}$	239.5	14 300	99(1)	1(1)	7
$ 04\rangle^{-}$	218.5	18 320	91(3)	9(3)	7, 9
$ 13\rangle^{-}$	239.5	14 790	16(6)	84(7)	7
$ 13\rangle^{-}$	218.5	18 800	6(5)	94(5)	7
$ 04^{-2}\rangle$	282	11 000	>98	<2	5
$ 05\rangle^{-}$	282	11 670	>98	<2	5

^aA sizable population in $v=2$ has been observed.

^bOnly OH($v=0$) product state was examined.

Sec. II, followed in Sec. III by quantum state resolved fragmentation results for H₂O excited to a series of $v_{\text{OH}}=2$ vibrational levels. These distributions are analyzed and discussed in Sec. IV, and interpreted in the context of simple QM models for the fragmentation event. The major conclusions are summarized in Sec. V.

II. EXPERIMENT

The essential experimental approach has been described in previous studies from this laboratory,^{10,16} and builds on powerful vibrationally mediated dissociation methods pioneered by Andresen and Crim.^{6,7,17} Water molecules are excited into specific rovibrational intermediate states with direct overtone pumping and then selectively photolyzed with 193 nm ultraviolet radiation. This excimer photolysis wavelength is close to optimal for Franck–Condon excitation of the outermost lobe of the wave function in the H₂O $A^1B_1 \leftarrow X^1A_1$ absorption band, which therefore suppresses UV absorption by unexcited water molecules present in the expansion by several orders of magnitude. The translational, vibrational, and rotational states of OH fragments are probed with laser induced fluorescence, providing information on the forces breaking the molecule apart during the photodissociation process. Experimental details relevant to the current study are briefly summarized in the following.

All experiments utilize a supersonic expansion of 1% of H₂O in a monoatomic carrier gas (He or Ar) at a total stag-

nation pressure of 50 Torr (1 Torr=1.333 22 mbar) through a pulsed slit valve (4 cm×125 μm, 10 Hz, 500 μs pulse duration). Even under these mild supersonic expansion conditions, H₂O cools down almost entirely into the lowest rotational states allowed by the nuclear spin statistics, $J_{K_a K_c} = 0_{00}$ (*para*) and 1_{01} (*ortho*), in a 3:1 ratio. The jet-cooled molecules are intersected 2 cm downstream with an infrared laser beam (5 ns pulse duration, 0.25 cm⁻¹ bandwidth), where the partial H₂O and total jet densities are 2×10^{13} and 2×10^{15} #/cm³, respectively. The IR laser can deliver up to 30 mJ/pulse to the jet region in a 5 mm² beam area. For a spectral pulse width of 0.25 cm⁻¹, this is sufficient to drive stronger $\nu_{\text{OH}}=2$ water overtone transitions nearly into saturation, resulting in vibrationally excited water densities approaching 10^{12} #/cm³. The long path length nature and slower $1/r$ density drop off of the slit expansion permits laser excitation, photolysis, and detection to occur efficiently over a much larger interaction region than would be accessible in a pinhole supersonic expansion geometry.

The IR laser (pump) pulse is followed in time by a counterpropagating ArF excimer laser (photolysis) pulse at 193 nm, delayed by approximately 20 ns from the pump. Typical photolysis laser energy in the intersection region is 1 mJ/pulse, with a 10 mm² cross section in the jet intersection area. Based on an estimated UV absorption cross section of $\approx 1.8 \times 10^{-21}$ cm²/#¹⁸ for ground state water molecules, a relative photodissociation probability of 2×10^{-5} is predicted for IR unexcited species. Empirically, we observe that for the strongest H₂O transitions in $\nu_{\text{OH}}=2$, the photodissociation signal is increased by 10^2 – 10^3 due to vibrationally mediated enhancement at 193 nm. Both the vibrationally mediated and direct 193 nm photolysis signals scale linearly with the excimer laser power, indicating that multiphoton processes and saturation effects are of negligible importance for the photolysis laser.

Fluorescence from the OH fragments is detected on the $A^2\Sigma \leftarrow X^2\Pi$ $v=1 \leftarrow 0$, $0 \leftarrow 0$ and $1 \leftarrow 1$ bands of OH. The probe radiation is produced by a frequency doubled dye laser (<0.1 cm⁻¹ bandwidth, Rhodamine 590) pumped by a frequency doubled Nd:YAG laser. The probe laser pulse (5 ns duration) is delayed by ≈ 20 ns from the photolysis pulse. To discriminate between vibrationally mediated and direct 193 nm photolysis events, the pump laser is operated at half the repetition rate, with the laser off and on triggers subtracted to generate a background-free IR-induced signal. To minimize saturation effects, the UV probe laser power is maintained well below 25 μJ/pulse for $v=0 \leftarrow 0/1 \leftarrow 1$ bands (<90 μJ/pulse for the $v=1 \leftarrow 0$ band) in an unfocused beam size of 30 mm² area that overfills both pump and photolysis beams. This results in partial saturation effects (<20%) for the strongest OH lines, which are explicitly corrected by normalizing with respect to a reference spectrum of collisionally thermalized OH. The thermalized OH sample is obtained under identical probe laser conditions by photolyzing a flowing 1–2 Torr mixture of N₂O, CH₄ and Ar through the vacuum chamber. Delays of >500 μs between the photolysis and probe pulses translate into over 3000 hard-sphere collisions, which ensures complete thermalization. By way of contrast, densities and time delays selected for the actual photolysis

studies correspond to fewer than 0.01 collisions of the nascent OH species.

The OH fluorescence is collected through an $f/1$ CaF₂ elliptical lens with a photomultiplier tube (PMT) positioned at right angles with respect to the supersonic expansion and collinear laser propagation axis. The pump and probe lasers propagate collinearly through the slit jet expansion, and are linearly polarized along the expansion axis. The OH fluorescence signal is sampled with a boxcar integrator, with scattered light attenuated by a 295 nm long pass and UV band-pass (UG-5) filters positioned in front of the PMT. Overall photon collection efficiency is a few percent, typically yielding 10^4 – 10^5 signal photons per laser pulse with all three lasers present. Laser powers, gas pulse intensities, and reference photoacoustic spectra are stored for normalization, diagnostics, and frequency calibration purposes. The detection efficiency for OH is estimated from signal-to-noise (S/N) resulting from 193 nm dissociation of H₂O. With the enhanced path length, density, and collection volume due to the slit expansion, detection sensitivities below 5×10^5 OH molecules per quantum state are routinely obtained.

The relevant spectroscopy for the laser induced fluorescence (LIF) detection of nascent OH product is as follows. Each rovibrational level of the ground electronic state of OH(²Π) is split into two spin-orbit components, $F_1 \equiv {}^2\Pi_{3/2}$ and $F_2 \equiv {}^2\Pi_{1/2}$. Each spin-orbit level is further split into two closely spaced Λ-doublets (A' and A''), which, in the high- J limit, can be correlated with the unpaired electron p -orbital lying in or perpendicular to the plane of rotation. The energy levels are labeled by \mathbf{J} (total angular momentum), overall parity, \mathbf{N} (total angular momentum excluding spin), symmetry with respect to the reflection through the plane of rotation ($A' \equiv \Pi^+$ and $A'' \equiv \Pi^-$), and additionally with spectroscopic e/f labels. For example, in this notation, ${}^2\Pi_{3/2}^+(5)$ refers to a state with $N=5$ in F_{1e} manifold with A' reflection symmetry, with rotational branches of the $A^2\Sigma(v') \leftarrow X^2\Pi(v'')$ bands labeled using notation $\Delta N_{F'F''}(N'')$, e.g., $Q_{21}(3)$. To achieve high oversampling in the data set, all 12 rotational branches with the exception of S_{21} are used in the data analysis, with each spin-orbit and Λ-doublet level independently probed on at least two branches.

III. RESULTS AND ANALYSIS

Figure 1 displays a sample action spectrum of jet-cooled H₂O between 7205 and 7310 cm⁻¹, obtained by tuning the probe laser to the top of the OH $Q_{11}(2)$ probe transition and scanning the IR pump laser frequency. All features in the spectrum result from vibrationally mediated dissociation of quantum state-selected H₂O in the jet-cooled expansion. The lines in this spectral range are therefore due to the transitions out of the lowest nuclear spin states ($J_{K_a K_c} = 0_{00}$ and 1_{01}) of H₂O, into rotational levels belonging to the $|02\rangle^-$ ($\equiv \nu_1 + \nu_3$ in normal mode representation) and $|02\rangle^+$ ($\equiv 2\nu_1$) vibrational modes. Throughout this paper, we will be using the $|mn^\pm k\rangle$ notation⁹ for H₂O vibrational states, where m and n represent local mode stretching quanta,¹⁹ and k (omitted for $k=0$) represents the quanta in the HOH bend. The strongest band, $|02\rangle^-$, is of A-type (i.e., $\Delta K_a = 0$, $\Delta K_c = \pm 1$) and can

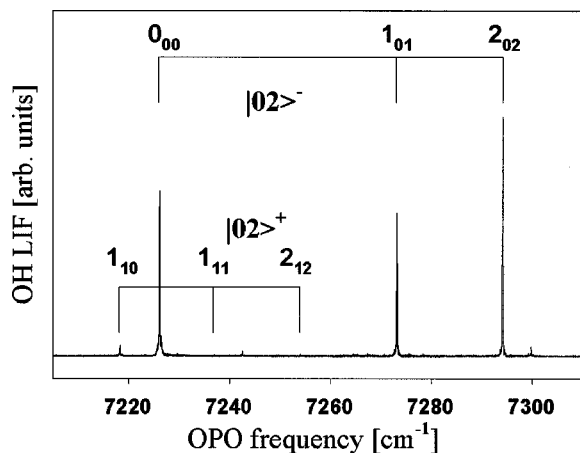


FIG. 1. Sample action spectrum obtained by scanning the IR probe laser over H₂O absorption lines within the $\nu_{\text{OH}}=2$ vibrational manifold. The probe laser is fixed on the $\nu=1\leftarrow 0$ Q₁₁(2) line of OH. Transitions from $J_{K_a K_c}=0_{00}$ and 1_{01} states of H₂O into rotational levels of $|02\rangle^-$ and $|02\rangle^+$ vibrations are observed in the displayed spectral range. The remaining weak transitions are due to incompletely cooled rotational levels of $|02\rangle^-$ state (such as $J_{K_a K_c}=1_{10}$). The relative intensities of peaks in the action spectrum depend on: (i) relative populations of H₂O states; (ii) state-to-state infrared absorption cross sections; (iii) UV photolysis cross sections; (iv) photodissociation quantum yields of OH into the ${}^2\Pi_{3/2}(N=2)$ probe state.

therefore access 0_{00} , 1_{01} , 2_{02} , and 2_{20} rotational levels (the $2_{20}\leftarrow 1_{01}$ transition lies outside the frequency range shown in Fig. 1). The corresponding $|02\rangle^+$ band is of B-type (i.e., $\Delta K_a = \pm 1$, $\Delta K_c = \pm 1$); it is an order of magnitude weaker and accesses a different subset of rotational levels: $1_{11}\leftarrow 0_{00}$, $2_{10}\leftarrow 1_{01}$, and $2_{12}\leftarrow 1_{01}$. The remaining weak lines in the action spectrum labeled with asterisks are straightforwardly assigned to $|02\rangle^-$ transitions from incompletely cooled H₂O 1_{10} rotational state (e.g., the transition at ≈ 7300 cm⁻¹ is $2_{11}\leftarrow 1_{10}$). Such "hot" transitions can be purposely enhanced by less efficient rotational cooling in pure He diluent versus Ar expansions. Approximately 300 cm⁻¹ to the red of these $|02\rangle^+$ and $|02\rangle^-$ bands, another two weak groups of lines can be assigned to combination bands of symmetric and asymmetric stretch fundamentals with two quanta of bending excitation, $\nu_1 + 2\nu_2$ and $\nu_3 + 2\nu_2$ in normal mode notation, and referred to in local mode notation as $|01^-2\rangle$ and $|01^+2\rangle$. Finally, an extremely weak band (down in intensity by 400 compared to $|02\rangle^-$) due to $|11\rangle^+$ is observed at around 7400 cm⁻¹, corresponding to the overtone of the asymmetric OH stretch ($2\nu_3$), but still accessible with quite respectable S/N ≈ 10 in the slit jet apparatus.

Access to this broad range of intermediate states permits one to investigate photodissociation dynamics from a family of energetically similar but physically quite distinct vibrational intermediates. For example, one might expect photodissociation of H₂O via excited bending states ($\nu_2 > 0$) to produce hotter OH rotational excitation.^{5,9} Similarly, the $|11\rangle^+$ state has its OH stretch excitation more equally distributed between the two equivalent OH bonds; based on the spectator model, therefore, one might predict significantly more OH($\nu=1$) vibrational excitation from $|11\rangle^+$ photodissociation compared to either $|02\rangle^+$ or $|02\rangle^-$ states. These effects will be discussed in more detail in the following. In

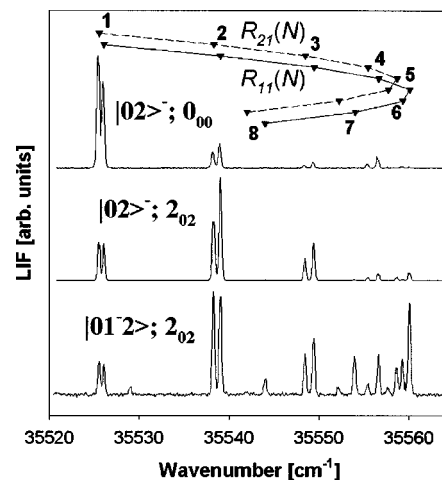


FIG. 2. Sample ${}^2\Sigma(v=1)\leftarrow {}^2\Pi(v=0)$ LIF probe spectra of OH photofragments. Only the R_{11} and R_{21} branches are displayed, probing ${}^2\Pi_{3/2}^+(N)$ levels of OH. From top to bottom, the intermediate H₂O state systematically changes from (a) $|02\rangle^-$ with no rotation, (b) $|02\rangle^-$ with two quanta of rotation, and, finally, (c) two quanta of both rotation and bending excitation. Note the increase in photofragment rotational excitation, due to projection of H₂O bending and rotational motion onto the asymptotic states of OH.

particular, we find both qualitative successes and failures of these spectator model predictions at such low polyad numbers.

By fixing the IR pump laser on a specific feature in the H₂O action spectrum and scanning the probe laser, a fluorescence excitation spectrum of the OH photofragments is obtained. Figure 2 shows sample portions of such spectra extending over the $R_{11}+R_{21}$ branches in the $\nu=1\leftarrow 0$ band of OH. Both branches probe the ${}^2\Pi_{3/2}^+(N)$ rotational manifold of OH. The top panel corresponds to photodissociation via the rotationless $|02\rangle^- 0_{00}$ intermediate state. The lower two panels, $|02\rangle^- 2_{02}$ and $|01^-2\rangle 2_{02}$, correspond to progressively increasing amounts of rotational and bending excitation, respectively. Note that the relative intensities of individual OH rotational transitions are quite different for these three intermediate states of H₂O. The $|01^-2\rangle 2_{02}$ state of H₂O, which has both bending and rotational degrees excited, clearly results in the most energetic distribution. To verify that the populations are indeed nascent, the stagnation pressure and the photolysis-probe delay have been increased by more than an order of magnitude without affecting the relative intensities in the spectrum. This is fully consistent with only $\approx 1\%$ probability of hard-sphere collisions between the OH photolysis fragment ($\nu_{\text{OH}} \approx 1.2 \times 10^5$ cm/s) and the carrier gas expected for the present experimental conditions.

From probe scans extending over 11 branches characteristic of the OHA ${}^2\Sigma\leftarrow X^2\Pi$ vibrational bands (all possible branches except S_{21}), the relative populations of *all* rotational, spin-orbit, and Λ -doublet states of OH can be obtained for a given rovibrational intermediate state. Complete OH fluorescence excitation spectra have been recorded for strong $|02\rangle^-$, $|02\rangle^+$, and $|01^-2\rangle$ intermediate vibrational levels of H₂O, for each of several rotational states accessible out of $J_{K_a K_c}=0_{00}$, 1_{01} . Due to the 200-fold weaker²⁰ IR cross sections relative to $|02\rangle^-$, only a limited set of populations in ${}^2\Pi_{3/2}^\pm$ OH manifolds have been examined for exci-

TABLE II. Percent OH rotational, spin-orbit, and lambda-doublet state populations from vibrationally mediated 193 nm photolysis of H₂O. Uncertainties (in parentheses) represent 2 standard deviations, evaluated from multiple independent data runs.

OH state	<i>N</i>	$ 02\rangle^-$ 0 ₀₀	$ 02\rangle^-$ 1 ₀₁	$ 02\rangle^-$ 2 ₀₂	$ 02\rangle^-$ 2 ₂₀	$ 02\rangle^+$ 1 ₁₀	$ 02\rangle^+$ 1 ₁₁	$ 02\rangle^+$ 2 ₁₂	$ 01^-2\rangle$ 0 ₀₀	$ 01^-2\rangle$ 1 ₀₁	$ 01^-2\rangle$ 2 ₀₂
${}^2\Pi_{3/2}^+$	1	19.5(6)	11.2(2)	4.29(35)	12.8(16)	0.46(14)	6.93(28)	15.0(13)	6.66(31)	3.20(12)	1.47(29)
	2	2.82(15)	6.48(29)	9.0(5)	3.5(4)	12.7(9)	7.7(9)	2.45(10)	0.63(6)	2.13(26)	3.87(12)
	3	0.57(5)	1.13(33)	2.58(14)	9.6(11)	2.2(5)	2.26(8)	3.5(4)	0.35(4)	0.78(6)	1.76(3)
	4	0.88(9)	0.71(4)	0.61(4)	2.8(9)	0.71(9)	0.74(5)	1.03(14)	2.44(3)	1.17(4)	0.98(4)
	5	0.061(9)	0.27(3)	0.61(2)	0.19(5)	0.58(2)	0.48(2)	0.29(7)	0.32(4)	0.89(14)	2.15(33)
	6	0.12(3)	0.074(10)	0.072(2)	0.37(14)	0.08(2)	0.22(3)	0.28(3)	1.48(11)	0.61(2)	0.78(9)
	7	0.04(1)	0.069(8)	0.072(7)	0.15(8)	0.15(3)			0.64(8)	0.44(2)	0.77(6)
	8			0.032(5)	0.05(3)				0.15(3)	0.19(2)	0.48(2)
	9								0.16(5)		0.20(5)
	10								0.021(5)		0.20(2)
${}^2\Pi_{3/2}^-$	1	2.01(19)	6.94(34)	12.6(9)	5.9(5)	21.3(19)	11.0(5)	2.4(6)	0.59(13)	3.03(8)	4.0(10)
	2	17.3(4)	11.4(1)	6.63(36)	15.4(3)	4.5(6)	9.7(17)	14.3(8)	5.6(7)	2.14(18)	0.95(6)
	3	11.0(4)	11.2(3)	10.6(6)	10.2(11)	10.7(23)	6.9(19)	6.4(5)	1.99(15)	1.98(3)	1.86(42)
	4	1.65(7)	3.84(17)	7.1(6)	4.3(1)	7.0(10)	6.4(13)	6.7(6)	1.65(16)	4.89(40)	6.6(7)
	5	5.0(4)	4.64(18)	2.17(11)	5.9(4)	1.80(11)	2.52(6)	3.90(7)	17.7(13)	11.2(6)	4.19(8)
	6	0.30(2)	1.05(25)	1.80(25)	0.47(9)	0.81(28)	0.78(45)	0.46(6)	1.48(40)	8.30(8)	11.8(5)
	7	0.93(13)	0.73(4)	0.61(3)	0.74(2)	0.095(10)	0.78(4)	2.10(37)	10.5(13)	7.5(8)	5.17(20)
	8	0.34(3)	0.47(3)	0.62(3)	0.21(9)	0.77(17)	0.61(17)	0.19(10)	6.1(16)	6.69(43)	6.20(30)
	9	0.047(9)	0.061(5)	0.20(3)	0.07(2)	0.14(3)	0.32(9)	0.55(20)	0.78(5)	1.3(7)	2.85(46)
	10	0.064(4)	0.041(5)	0.046(6)	0.047(8)			0.09(3)	1.23(9)	1.28(21)	0.35(8)
	11			0.035(5)							
${}^2\Pi_{1/2}^-$	1	0.76(7)	3.23(23)	5.6(5)	0.77(14)	8.6(5)	7.2(19)	1.45(16)	0.18(6)	1.29(19)	1.85(36)
	2	10.7(8)	7.95(60)	3.94(20)	5.4(7)	1.92(24)	7.3(14)	10.6(21)	2.6(8)	1.46(2)	0.85(3)
	3	5.83(26)	7.71(12)	6.3(5)	3.80(15)	6.5(8)	5.8(5)	3.8(6)	0.89(20)	1.25(6)	1.32(1)
	4	1.18(4)	2.32(16)	5.0(5)	2.63(22)	4.01(30)	6.11(31)	4.2(6)	0.88(11)	4.26(39)	5.3(6)
	5	3.34(33)	3.00(12)	1.59(11)	2.6(4)	0.72(5)	1.51(36)	2.4(5)	9.7(12)	7.4(5)	2.1(8)
	6	0.60(7)	1.25(10)	2.42(6)	0.44(5)	2.1(5)	1.81(4)	0.98(11)	1.40(11)	6.6(5)	9.1(8)
	7	0.63(7)	0.55(2)	0.47(4)	0.44(5)	0.17(4)	0.60(8)	1.67(33)	9.3(27)	4.92(19)	3.83(4)
	8	0.31(8)	0.43(3)	0.58(5)	0.24(9)	0.54(29)	0.50(7)	0.20(4)	3.83(26)	4.9(20)	5.2(5)
	9	0.038(2)	0.065(3)	0.17(1)	0.068(5)	0.11(4)	0.23(5)	0.48(15)	0.39(7)	0.82(19)	3.1(9)
	10	0.037(4)	0.055(4)	0.042(7)	0.074(5)				1.6(6)	1.18(37)	0.48(2)
	11									0.25(8)	0.75(7)
	12										0.13(5)
${}^2\Pi_{1/2}^+$	1	9.25(41)	6.1(4)	2.33(24)	3.35(19)	0.40(19)	3.28(5)	7.4(13)	4.3(8)	2.44(17)	1.2(7)
	2	1.45(14)	3.97(14)	7.5(7)	1.52(11)	7.4(18)	5.08(20)	1.61(10)	0.39(3)	1.92(2)	2.30(24)
	3	1.44(21)	1.51(9)	2.11(29)	3.28(13)	1.30(26)	1.85(5)	3.4(12)	0.56(21)	0.40(11)	0.92(6)
	4	1.21(15)	1.02(8)	1.16(15)	2.03(26)	1.22(36)	0.79(6)	0.95(11)	1.11(4)	0.60(6)	0.66(19)
	5	0.18(2)	0.29(2)	0.75(5)	0.25(7)	0.71(16)	0.59(20)	0.52(13)	0.26(5)	0.68(5)	1.47(20)
	6	0.26(3)	0.25(1)	0.15(1)	0.32(4)	0.16(6)		0.38(9)	1.03(24)	0.70(4)	0.77(2)
	7	0.077(19)	0.095(6)	0.18(2)	0.12(1)	0.27(2)		0.11(5)	0.32(5)	0.60(7)	1.13(15)
	8	0.029(5)	0.0087(5)	0.058(11)	0.059(13)			0.10(5)	0.45(8)	0.48(8)	0.57(17)
	9			0.025(5)	0.04(1)				0.34(5)	0.22(2)	0.32(2)
	10			0.017(5)							0.073(6)

tation into $|11\rangle^+$ state. To enhance the statistics, each spectrum is collected two to five times and analyzed independently. Lines in all spectra are integrated and the resulting areas least-square fitted using OH populations as adjustable parameters. The required individual rotational transition strengths are taken from Chidsey and Crosley database²¹ and small saturation correction factors are explicitly determined from the reference room-temperature OH spectra on a line-by-line basis. Since all populations are statistically quite overdetermined (each level is probed by up to three independent branches), the least-squares fitting is extremely robust. Although accidental line overlaps do occur [e.g., $R_{22}(3)$ line is blended with the $Q_{11}(1)+Q_{21}(1)$ doublet in the $v=1\leftarrow 0$ band], the low power and relatively high

resolution of the probe laser reduce such overlaps to a minimum. The linewidths in the recorded spectra are limited by the Doppler broadening with full width at half maximum $\approx 0.3\text{ cm}^{-1}$, i.e., consistent with the expected OH translational energy release. The fitted populations for OH($v=0$) are summarized in Table II, wherein the results and uncertainties are obtained as a weighted average of populations from several independent data runs. OH($v=1$) populations are not listed because they were recorded only for a limited subset of states within ${}^2\Pi_{3/2}^\pm$ OH manifolds to verify that OH rotational and vibrational distributions are decoupled from each other (see the following).

Of particular interest in this work is the fractional branching into OH($v=1$) and OH($v=0$) products as a func-

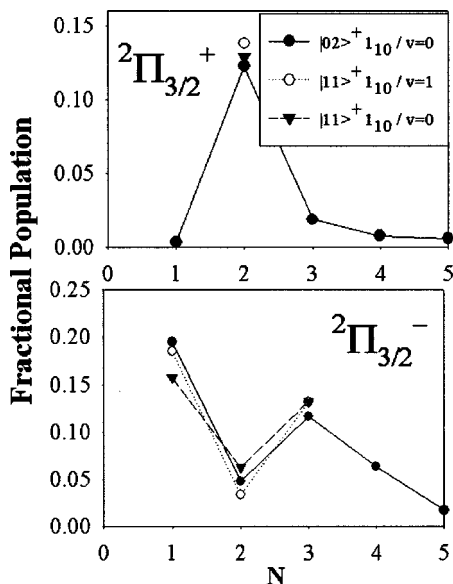


FIG. 3. A subset of relative OH($v=1$) and OH($v=0$) populations in $2\Pi_{3/2}^{\pm}$ manifolds resulting from UV photolysis of $|02\rangle^{+}1_{10}$ and $|11\rangle^{+}1_{10}$ states of H₂O. Strong similarities in the observed distributions support the assumption of decoupling between vibrational and rotational degrees of freedom in OH photofragments (this assumption is used to derive relative final vibrational populations of OH listed in Table I).

tion of H₂O rovibrational intermediate states, which are examined in a separate experiment by comparing repeated scans over the $Q_{11}(3)$ line, which probes the $2\Pi_{3/2}^{-}(3)$ level in OH, for the $v=1\leftarrow 1$ and $v=0\leftarrow 0$ subbands, for a series of intermediate states and range of IR pump powers. Relative transition probabilities for these $v=1\leftarrow 1$ and $v=0\leftarrow 0$ subbands are taken from Ref. 21. This ratio could in principle be further corrected for fractional $v=1$ versus $v=0$ population in the initial $2\Pi_{3/2}^{-}$ manifold level. In practice, however, the rotational, spin-orbit, and lambda-doublet distributions appear to be strongly uncoupled from the OH(v) vibrational state, despite a clear sensitivity to different intermediate rotational states. For example, Fig. 3 shows a comparison between relative OH($v=1$) and OH($v=0$) populations in $2\Pi_{3/2}^{\pm}$ manifolds resulting from UV photolysis of $|02\rangle^{+}1_{10}$ and $|11\rangle^{+}1_{10}$ states of H₂O. The lambda-doublet and rotational populations are the same within the experimental precision. Therefore, the nascent vibrational populations of OH integrated over each manifold can be reliably estimated from comparison of a single rotational line in the $2\Pi_{3/2}^{-}$ manifold for $v=1\leftarrow 1$ and $v=0\leftarrow 0$ OH transitions (as long as the same rotational state of H₂O is photolyzed). The results of these measurements are listed in Table I, put explicitly into context with OH($v=1$)/OH($v=0$) branching ratios obtained from all vibrationally mediated dissociation studies to date.

IV. DISCUSSION

A. Nascent OH rotational populations

A particularly striking observation from previous vibrationally mediated dissociation studies^{5-7,9,10} has been the presence of strong oscillations in OH nascent populations as

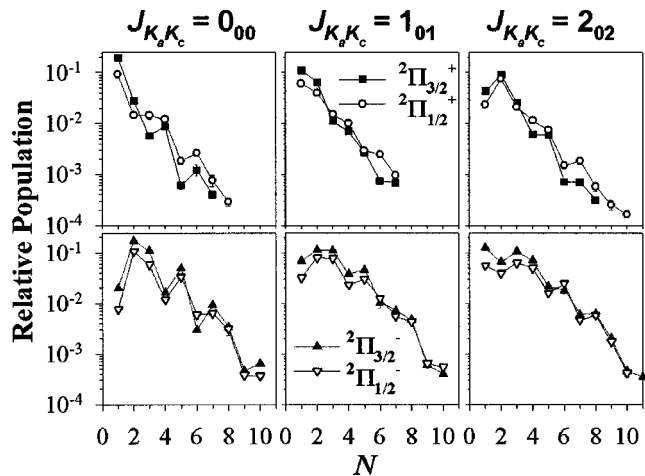


FIG. 4. Effect of initial H₂O($|02\rangle^{-}$) rotation on the observed OH distributions. The distributions are plotted as a function of N for each spin-orbit and Λ -doublet rotational manifolds. The oscillations of populations vs N are pronounced even on the logarithmic scale. Notice that there is little difference in the populations of the two spin-orbit components ($2\Pi_{1/2}$ vs $2\Pi_{3/2}$) but an appreciable difference between the A' and A'' Λ -doublets. The rotational state of H₂O($|02\rangle^{-}$) changes from 0_{00} to 1_{01} to 2_{02} from left to right, which has the effect of slightly increasing the average rotational energy of OH fragments.

a function of rotational state. Such oscillations in the nascent OH distributions are also quite evident in the present study of the $v=2$ polyad (Table II). By way of example, Fig. 4 displays experimental OH populations versus N for each spin-orbit and Λ -doublet manifolds for photodissociation of H₂O($|02\rangle^{-}$) in a series of intermediate rotational states, which indicate clear oscillations even on a logarithmic scale. Interestingly, these trends are remarkably similar for the two spin-orbit components ($2\Pi_{1/2}$ and $2\Pi_{3/2}$) for each lambda-doublet manifold, whereas appreciably larger differences are apparent between the A' versus A'' Λ doublets. It is worth noting that the population data for different spin-orbit manifolds are obtained from entirely independent rotational branches; the systematic agreement between $2\Pi_{1/2}$ and $2\Pi_{3/2}$ traces, therefore, provides additional support for the high S/N and reproducibility of our data.

The origin of these oscillations in OH population^{1,3,5,8,10,12,22} has been thoroughly discussed, and it arises from quantum mechanical interference between the various OH outgoing spin-orbit and lambda-doublet product channels. As a simple zeroth-order prediction, this would suggest a much smoother distribution when summed over all interfering channels. This prediction is tested in Fig. 5, which displays OH photofragment distributions resulting from photodissociation of H₂O via $|02\rangle^{-}J_{KaKc}=2_{02}$, nicely confirming the interference nature of the photodissociation process. Specifically, while populations within a given individual spin-orbit/ Λ -doublet manifold [Fig. 5(a)] are highly non-monotonic functions of J_{OH} , the sum over these manifolds [Fig. 5(b)] is much more consistent with a smooth rotational distribution, arising from largely complete cancellation between the Λ^{+} and Λ^{-} doublets contributions. This behavior is echoed in distributions for each of the intermediate rota-

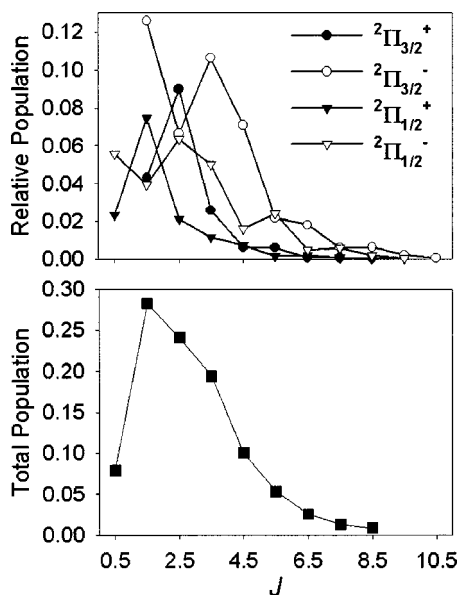


FIG. 5. OH photofragment distributions resulting from photodissociation of $\text{H}_2\text{O}(|02\rangle^-)$ in 2_{02} rotational state plotted as a function of J_{OH} . While the populations within the individual spin-orbit and Λ -doublet manifolds (top panel) strongly oscillate with J_{OH} , the total population (bottom panel) is much smoother reflecting the interference nature of the photodissociation.

tional states of water from this study, as can be verified from a detailed investigation of Table II.

The theoretical framework developed by Balint-Kurti, Schinke, and others^{1,3,5,8,10,12,22} to explain such trends is that the OH nascent state distribution reflects a Franck-Condon-type projection of the intermediate state wave function on the upper potential surface, followed by wave packet evolution in the exit channel out toward asymptotic products. Based on this picture, one would expect a relatively strong dependence of $\text{OH}(v)$ populations on H_2O intermediate vibrational state, and, conversely, OH rotational state populations relatively insensitive to intermediate state vibrations of the same local mode character. Striking support for the former assertion is evident in Fig. 6, which shows nascent populations for the $2\Pi_{3/2}^\pm$ manifolds, obtained for a progression of increasingly OH stretch excited polyad states (e.g., $|0n\rangle^-$, $n=1-5$) out of $J_{K_a K_c}=0_{00}$. Although the excess energies for the H_2O states in Fig. 6 vary by more than a factor of 2 (Table I), the N dependence of the distributions within a given spin-orbit and Λ -doublet manifold remains nearly identical. Photodissociation of H_2O from a series of vibrational states with nonzero angular momenta yields results that follow similar trends, although subtle differences between the OH distributions start to appear already at $J=1$.¹⁰

In the context of such a Franck-Condon picture, one would expect overall rotation of the H_2O prior to photodissociation to result in warmer OH rotational state distributions, as is indeed clearly evident in Fig. 4. Vibrational pre-excitation of HOH bending states would imply even stronger overlap on final OH rotation wave functions, and thus a Franck-Condon picture for photolysis would predict a much hotter rotational distribution. This prediction is directly confirmed in Fig. 7, which compares rotational populations resulting from the photolysis of H_2O in $|02\rangle^-$ and $|01^-2\rangle$

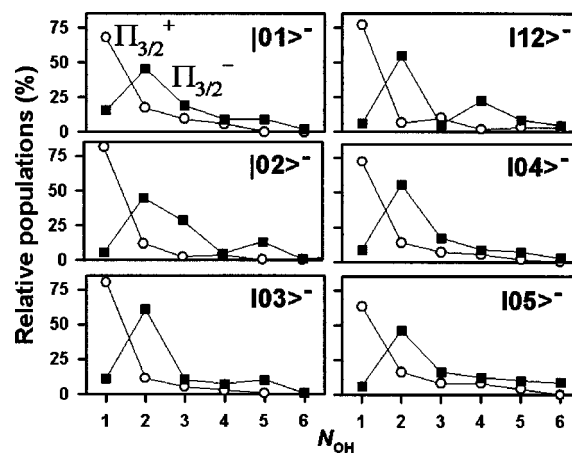


FIG. 6. Populations of $2\Pi_{3/2}^+$ (open circles) and $2\Pi_{3/2}^-$ (closed squares) states of OH in photodissociation of different vibrational states ($v_{\text{OH}}=1$ to 5) of H_2O in $J_{K_a K_c}=0_{00}$. Although the photodissociation is probed at very different excess energies (see Table I), the gross features of the rotational distributions are strikingly similar, due to the good separability of vibrational and rotational time-scales for the motion.

states, with the latter clearly resulting in a much more rotationally energetic OH distribution. However, in spite of large differences in populations, a more detailed inspection reveals clear similarities in the oscillatory structure. For example, the $2\Pi^-$ distributions for $|02\rangle^-0_{00}$ and $|01^-2\rangle0_{00}$ intermediate states (Fig. 7, lower panels) exhibit local maxima (at $N=2, 5, 7$) and minima (at $N=1, 4, 6, 9$), despite quite clear differences in the overall smoother trend. Such behavior is in fact consistent with a Franck-Condon picture, reflecting the approximate separability of the rotational-bending wave function for the H_2O intermediate state. Specifically, the rotational wave function is predominantly responsible for the fast oscillations, while the bending wave function dictates the overall shape of the OH distribution.

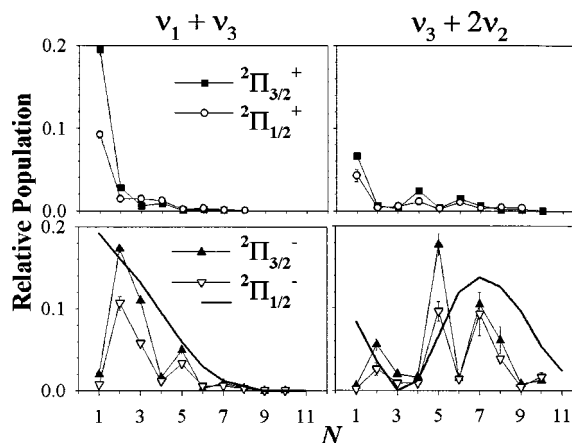


FIG. 7. Effect of H_2O bending excitation on the OH rotational distribution. The distributions are plotted as a function of N for each spin-orbit and Λ -doublet rotational manifold. The panels on the left and right show data for $|02\rangle^-$ and $|01^-2\rangle$, respectively. Although the bending excitation of H_2O significantly increases the OH rotation, the nonmonotonic structure on top of the distributions is quite similar. The solid curves in the bottom panels correspond to the Franck-Condon projections of the H_2O bending wave functions on the OH rotational states (Ref. 9).

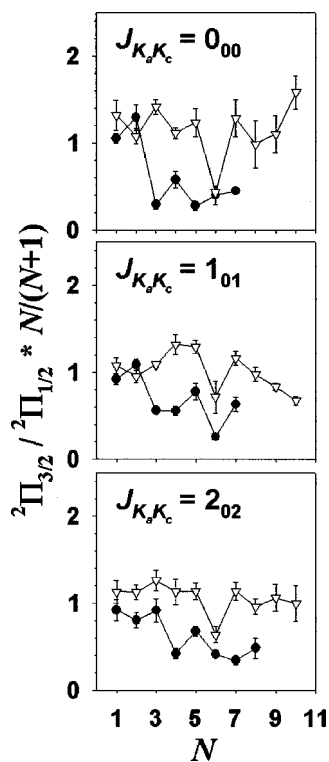


FIG. 8. Relative populations of OH spin-orbit states in photodissociation of H₂O($|02\rangle^-$). Triangles and closed circles represent the ratios $[^2\Pi_{3/2}(N)]/[^2\Pi_{1/2}(N)] * N/(N+1)$ for A'' and A' Λ -doublets, respectively. The $N/(N+1)$ multiplier accounts for the $2J+1$ space degeneracy; the high-temperature statistical limit would correspond to $N/(N+1)=1$.

More quantitatively, one can model this second contribution by projecting the HOH bending wave function onto the asymptotic OH rotational states.^{1,5,9} This leads to a distribution proportional to

$$\sin^2\left(j\gamma_e + (-1)^k \frac{\pi}{4}\right) \phi_k^2\left(\frac{j}{\bar{m}\omega_{\text{HOH}}}\right),$$

where ϕ_k is the HOH bending wave function for k quanta of excitation, j is the rotational angular momentum of OH fragment, γ_e is the equilibrium bond angle in H₂O, ω_{HOH} is harmonic frequency for the bending motion, and \bar{m} is the effective reduced mass for the bending motion.⁹ Figure 7 shows the nonoscillatory part of the Franck-Condon distribution for $k=2$ compared with the experimental data obtained for the $|01^-2\rangle$ state of H₂O. The data are in excellent agreement with this simple model, especially in reproducing the slow nodal structure around $N=3$ and a secondary maximum at $N=7$.

B. Nascent OH spin-orbit and lambda-doublet distributions

As shown above, spin-orbit and lambda-doublet states have already proven important in generating quantum interference effects between outgoing exit channels. However, they also provide additional dynamical information on the photolysis event. Figure 8 shows the population ratio of the two spin-orbit components, $[^2\Pi_{3/2}(N)]/[^2\Pi_{1/2}(N)] * N/(N+1)$, and its variation with N and Λ -doublet symmetry,

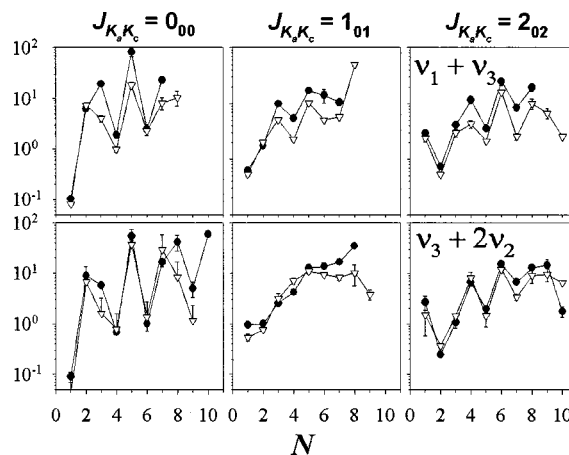


FIG. 9. Relative populations of OH Λ -doublets in photodissociation of H₂O. The top three panels are for 0_{00} , 1_{01} , and 2_{02} rotational states of H₂O($|02\rangle^-$) and the bottom panels are for the same rotational states of H₂O($|01^-2\rangle$). Closed circles and open triangles represent $^2\Pi_{3/2}^-(N)/^2\Pi_{1/2}^+(N)$ and $^2\Pi_{1/2}^-(N)/^2\Pi_{3/2}^+(N)$, respectively. The ratios are quite similar for the two vibrational states but are sensitive to H₂O angular momentum. Faster water rotation results in a smaller difference between the positive and negative OH Λ -doublets.

where the $N/(N+1)$ coefficient includes the $2J+1$ space degeneracy. In the statistical regime, $[^2\Pi_{3/2}(N)]/[^2\Pi_{1/2}(N)] * N/(N+1)$, should eventually reach unity for high N . Indeed, this statistical limit is what was observed in early 157 nm photolysis of room temperature H₂O¹¹ as well as 193 nm photolysis of H₂O in $0_{00}|01^-$ state.^{6,8} However, as shown in Fig. 8, this is not in good agreement with the current 193 nm photolysis study of H₂O in the $v=2$ polyad, where sizable N -dependent deviations from unity are evident out at high rotational levels with high S/N. Supporting results were also observed in previous photodissociation studies of H₂O in the $v_{\text{OH}}=3$ polyad, which revealed sizable deviations from the statistical limit.¹⁰ At the present time, there is no theoretical understanding for the predominance of $\Pi_{3/2}$ states in the asymmetric (A'') manifold and $\Pi_{1/2}$ states in the symmetric (A') manifold. In fact, the data might suggest a trend away from statistical behavior in nascent spin-orbit distributions as a function of H₂O polyad number, though this issue awaits more detailed theoretical investigation.

The Λ -doublet ratio of asymmetric (A'') to symmetric (A') OH product states has been of special dynamical interest. In the limit of zero spin-orbit interaction (which is valid for sufficiently high OH rotational levels), the electronic transition symmetry in H₂O should strongly favor production of A'' states of OH. A rapid increase in the $[\text{OH}(A'')]/[\text{OH}(A')]$ ratio with N has indeed been observed in several previous studies of photodissociation of H₂O and its general shape is now reasonably well understood, at least in the absence of the parent rotation.^{11,16} The Λ -doublet ratios from the present study for two intermediate vibrational states ($|02\rangle^-$ and $|01^-2\rangle$) and several rotational states of H₂O are shown in Fig. 9 (note the logarithmic axis). In interesting contrast to the OH rotational energy distribution, which strongly depends on the parent bending state, the $[\text{OH}(A'')]/[\text{OH}(A')]$ ratio appears to be remarkably insen-

sitive to the vibrational state of H₂O. The magnitudes and phases of oscillations in this ratio are now in very close agreement for $|02\rangle^-$ and $|01^-2\rangle$, as well as for all pairs of H₂O rotational states considered. This is again consistent with a simple Franck–Condon separability of bending and rotational wave functions; the bending wave function influences only the N dependent features of the OH distribution and not preferential formation of specific parity levels.

As a final note, these results make for interesting comparison with previous 157 nm photolysis studies of room temperature H₂O,¹¹ which exhibit a surprising *absence* of any Λ -doublet inversion ratio. It has been previously argued that this “smearing out” of the Λ -doublet population inversion for room temperature samples may be the result of orbital mixing caused preferentially by out-of-plane rotational motion of H₂O.^{11,16} Indeed, the data in Fig. 9 show clear Λ -doublet inversion for the series of $J_{K_a K_c} = 0_{00}, 1_{01}, 2_{02}$ H₂O rotational states, which would correspond classically to increasing *in-plane* versus out-of-plane rotational versus motion. However, close examination of Table II indicates that similar Λ -doublet inversion behavior is observed for photolysis from both 2_{02} and 2_{20} levels (i.e., the two classical extremes of in-plane and out-of-plane rotational motion), suggesting that such an orbital mixing effect is not important, at least for small angular momentum values.

C. OH vibrational distributions

A particularly relevant aspect of this study is the ability to investigate vibrational state symmetry effects on H₂O photodissociation dynamics, as well as the potential breakdown of the spectator model in vibrationally mediated photolysis events. First of all, as noted in Sec. II, previous studies have focused on a subset of high overtone vibrations, specifically antisymmetric (i.e., *ungerade*) states and typically with strongly local mode character due to anharmonic limitations on vibrational overtone intensities. At the $v_{\text{OH}} = 2$ overtone level, these anharmonic effects are less important, yielding sufficient oscillator strength for probing photolysis events from each member of the polyad, $|02\rangle^+$, $|11\rangle^+$, and $|02\rangle^-$, including both *gerade* and *ungerade* states. Second, $v_{\text{OH}} = 2$ is the lowest polyad with sufficient rearrangements of vibrational quanta to distinguish between cleaved and surviving bonds in the photolyzed H₂O. This offers a unique opportunity to test the spectator paradigm down at low levels of vibrational excitation. It is worth noting that predictive understanding of such effects at low vibrational quanta on chemical reaction dynamics is particularly relevant, for example, in thermal models of combustion phenomena. Finally, despite the 50% weaker initial vibrational excitation in the H₂O intermediate state, 193 nm photolysis of these first overtone $|02\rangle^+$, $|11\rangle^+$, and $|02\rangle^-$ levels sample comparable upper state energies as previous studies of $|04\rangle^-$ and $|13\rangle^-$ states by Vanderwal *et al.*⁷ As a result, this allows the present study to focus selectively on the influence of symmetry and intramolecular nodal distribution on the photolysis dynamics.

Inspection of Table I reveals two important facts. First observation is that photodissociation of *gerade* $|11\rangle^+$ and

$|02\rangle^+$ states produces substantially more vibrational excitation in OH compared to that of the *ungerade* $|02\rangle^-$ state. Specifically, one finds significant levels of vibrational excitation from both $|02\rangle^+$ and $|11\rangle^+$, with $[\text{OH}(v=0)]:[\text{OH}(v=1)]=0.63(3):0.37(3)$ and $0.47(5):0.53(5)$, respectively; these results are in clear contrast to nearly quantitative 98% yield of OH($v=0$) from $|02\rangle^-$. This observation is consistent with time-dependent wave-packet simulations,^{23,24} which predict significant differences in the photodissociation dynamics of *ungerade* and *gerade* states of H₂O. Specifically, wave packets prepared from *ungerade* states are predicted to evolve initially along the asymmetric stretch coordinate, whereas *gerade* state wave packets have an appreciable initial component along the symmetric stretch. This difference shows up as a 19 fs recurrence in the wave-packet autocorrelation function, which is found for all *gerade* states but does not occur for *ungerade* ones.²⁴ Physically, displacement on the upper surface along the symmetric stretching coordinate corresponds to motion *perpendicular* to the minimum energy path. Such motion would predict enhanced vibrational excitation of the surviving OH bond, in good agreement with the current experimental observations.

A second, more subtle observation is that the OH vibrational distributions from $|11\rangle^+$ and $|02\rangle^-$ cannot be fully explained by adiabatic conservation of the vibrational nodal pattern in the undissociated H₂O bond. Indeed, this is the essence of the simple spectator model, which worked so beautifully for photodissociation of the higher $|04\rangle^-$, $|13\rangle^-$, $|03\rangle^-$, and $|12\rangle^-$ states of H₂O.^{1,7,10} Such a model assumes that the region of the excited PES sampled by the photolysis is characterized by weak interactions between the two OH bonds. Although the excess energies utilized in the current study fall in the expected range of validity of the spectator model,²⁴ the level of agreement with observed product OH vibrational excitation is clearly mixed. On one hand, the fractional yield of OH($v=1$) from dissociation of $|11\rangle^+$ ($53 \pm 5\%$) is significantly higher than that from $|02\rangle^-$ ($2 \pm 1\%$), in qualitative agreement with expectation. However, there is only a minimal difference (≈ 1.4 -fold) between $[\text{OH}(v=1)]/[\text{OH}(v=0)]$ product ratios resulting from photolysis of $|11\rangle^+$ and $|02\rangle^+$ states. This is in striking contrast with the $|13\rangle^-$ state behavior, which at 218.5 nm exhibited an order of magnitude more OH($v=1$) than $|04\rangle^-$.⁷ Even more to the point, there is an order of magnitude difference in OH($v=1,0$) photolysis behavior between $|02\rangle^+$ and $|02\rangle^-$ states, which is in clear contradiction to predictions from the spectator model.

To help identify the physical origin of these discrepancies, we have explicitly calculated two-dimensional (2D) wave functions for the bound and continuum OH(R_1, R_2) stretching states of H₂O. Specifically, the ground state wave functions are obtained from matrix diagonalization of a 2D distributed Gaussian basis set on the Sorbie–Murrell potential energy surface,²⁵ with the HOH bend angle fixed at 104.5° and eigenvalues converged by successively increasing basis set size. Similarly, the excited state wave functions are obtained by matrix diagonalization on the Staemmler–Palma potential surface,²⁶ for a uniformly distributed grid of Gaussian basis functions over the Franck–Condon region and ex-

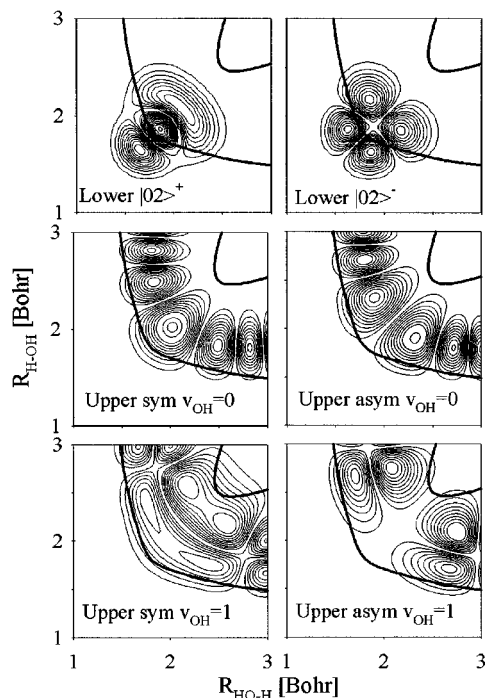


FIG. 10. Ground state ($|02\rangle^+$ and $|02\rangle^-$) and excited state symmetric/antisymmetric wave functions correlating with $\text{OH}(v=0,1)$ and accessed via excitation near 193 nm. Bold lines surround the energetically accessible Franck–Condon region for 193 nm excitation out of $v_{\text{OH}}=2$ H₂O states. Contours corresponding to positive and negative wave function values are shown in solid and dashed lines, respectively.

tending ($r_{\text{max}} \approx 10 a_0$) out into the entrance (HO+H) and exit (H+OH) channels. Out at r_{max} , the upper state eigenfunctions approximate the behavior of true continuum wave functions, whose asymptotic $\text{OH}(v)$ state can be readily identified by the nodal pattern. Such variational matrix procedures necessarily yield a discrete representation for the upper states, which makes it challenging to obtain quantitative Franck–Condon factors for transitions from symmetric and asymmetric states of water molecule at exactly the same energy. However, this does permit estimation of Franck–Condon factors appropriate to a finite bin of photolysis energies, and for wave functions correlating asymptotically with a specified $\text{OH}(v)$. In particular, this provides an excellent qualitative basis for interpretation of experimental observations, as demonstrated in the following.

The resulting lower state wave functions for $|02\rangle^+$ and $|02\rangle^-$ states of H₂O are shown in Fig. 10. Also shown are sample symmetric and antisymmetric upper state wave functions correlating asymptotically with $\text{OH}(v=0)$ and $\text{OH}(v=1)$, respectively. As anticipated, the upper state wave functions are confined to the saddle region on the upper PES energetically accessible via 193 nm excitation from $v_{\text{OH}}=2$; for the purposes of visualization, this area is enclosed in Fig. 10 by bold lines. From the Franck–Condon principle, the photodissociation dynamics will be dominated by wave function overlap in this classically accessible region.

Figure 10 offers a good zeroth-order picture for interpreting the observed trends. Specifically, due to a strong *outward* shift of the wave function along the symmetric stretch direction, the two lobes of the upper state wave function

correlating with $\text{OH}(v=1)$ overlap well with the *outer* two lobes for the $|02\rangle^+$ state. Conversely, the upper state wave function correlating with $\text{OH}(v=0)$ has only one lobe in the symmetric stretch direction, and furthermore, by virtue of lower asymptotic OH stretch energy, reaches further *inward* along the symmetric stretch coordinate. This moves the single upper state lobe over the oppositely signed lower state lobes of $|02\rangle^+$, yielding destructive interference of the Franck–Condon overlap. The result is a net *decrease* and *increase* in photolysis efficiency for formation of $\text{OH}(v=0)$ and $\text{OH}(v=1)$, respectively, as experimentally observed for the $|02\rangle^+$ lower state. The situation for the photolysis of $|02\rangle^-$ is precisely reversed, with the outer two lobes of the $|02\rangle^-$ wave function now overlapping well with the upper state wave function correlating with $\text{OH}(v=0)$. Additionally, $|02\rangle^-$ overlap with the upper state wave function correlating with $\text{OH}(v=1)$ is much less efficient, due both to a node in the asymmetric stretch direction and a larger displacement between lobe centers in the upper state. The net effect is now an *increase* and *decrease* in photolysis efficiency for formation of $\text{OH}(v=0)$ and $\text{OH}(v=1)$, respectively, again in good agreement with experimental observation for the $|02\rangle^-$ lower state.

This qualitative picture suggests that the success of the spectator model at *higher* quanta of excitation arises from anharmonic elongation of the lower state eigenfunctions along the dissociation coordinate. Since both lower and upper state potential surfaces have overlapping wells in the spectator OH stretch, this leads to relatively tight (i.e., parallel) registry of the upper and lower wave functions on the way toward dissociation. The spectator model then follows immediately from an effective one-dimensional Franck–Condon overlap in these elongated geometries, which is therefore quasideagonal in vibrational quanta along the spectator bond. On the other hand, these elongation effects become less important for lower quanta of excitation, and particularly so for the pure symmetric stretch overtone, i.e., $|02\rangle^+$. In this regime, Franck–Condon factors depend in detail on the energy dependent shift in registry between the upper and lower state wave functions along the symmetric stretch coordinate, which, as evidenced in this work, can lead to dramatic deviations from simple spectator model predictions.

An alternative interpretation of such nonspectator model predictions arises from the degree of localization in the H₂O vibrational modes. According to the calculations of Lawton and Child,²⁷ the stretching vibrations in H₂O are represented with the local mode basis set, $\psi_{mn}^{(\pm)} = 2^{-1/2} [\chi_m(R_1)\chi_n(R_2) \pm \chi_n(R_1)\chi_m(R_2)]$, where $\chi_n(R)$ are Morse eigenfunctions for the individual OH bonds in H₂O. Most relevantly, Lawton and Child showed that the H₂O vibrational Hamiltonian can be highly diagonal in this $\psi_{mn}^{(\pm)}$ basis, at least for high vibrational levels. For example, H₂O states $|04\rangle^-$, $|13\rangle^-$, and $|02\rangle^-$ are heavily dominated by $\psi_{04}^{(-)}$ (94.9%), $\psi_{13}^{(-)}$ (94.7%), and $\psi_{02}^{(-)}$ (99.9%), respectively (percent values in parentheses represent the squares of the coefficients in front of the respective basis functions). In fact, the majority of *ungerade* H₂O vibrational states can be well described by just one local mode basis function with only minor contami-

nation from other members of the basis. On the contrary, *gerade* states ($|02\rangle^+$ and $|11\rangle^+$), although still dominated by the respective local mode basis functions, tend to have much smaller degree of localization (79.7% and 79.6%, respectively).²⁷ The most important mixing terms have the form $\langle n \pm 1, m \mp 1 | H | n, m \rangle$ reflecting interactions between basis states differing by one vibrational quantum within the same polyad. Such increased coupling between the two bonds can therefore lead to one quantum changes in the vibrational state of the surviving OH bond. This is of course consistent with present observations that photolysis of $|02\rangle^+$ and $|11\rangle^+$ states, which each contain both $\psi_{02}^{(+)}$ and $\psi_{11}^{(+)}$ basis functions, produce more and less OH($v=1$), respectively, than predicted from a pure spectator model. In view of this, it would be interesting to examine photodissociation dynamics of vibrational states such as $|22\rangle^+$ and $|13\rangle^+$, which are even more poorly described by the local mode picture. Based on the present analysis, one would predict photolysis to produce a significant spread in OH(v) levels, mirroring the broader local mode content of the initial wave function. Although such states cannot be accessed from the ground state via a direct overtone excitation, they may be populated by means of two photon transitions as demonstrated in Ref. 28.

V. SUMMARY

193 nm photodissociation dynamics of gas-phase H₂O molecules has been examined from selected rotational and vibrational quantum states within the $v_{\text{OH}}=2$ polyad. Rotational, spin-orbit, and lambda-doublet quantum state distributions of the OH photofragments can be well described in the framework of previous theoretical and experimental studies at both higher and lower polyad numbers. However, the OH vibrational distributions deviate considerably from conventional spectator model predictions, which are based on assuming adiabatic conservation of vibrational quanta in the surviving OH bond. Instead, the data suggest a somewhat more restricted regime of applicability for the spectator model, specifically for vibrational states of H₂O at relatively high levels of local mode excitation. This breakdown of the spectator model is seen to be particularly strong for *gerade* states of the $v_{\text{OH}}=2$ polyad such as $|11\rangle^+$ and $|02\rangle^+$, both of which yield comparable photolysis branching into OH($v=0$) and OH($v=1$). This is in good agreement with theoretical wave-packet studies and can be rationalized by higher initial momentum projection along the symmetric stretch co-

ordinate for *gerade* state photolysis. This results in a greater departure from the minimum energy photolysis path and therefore enhanced vibrational excitation in the asymptotic OH.

ACKNOWLEDGMENTS

This work has been funded by support from the National Science Foundation and the Air Force Office of Scientific Research.

- ¹V. Engel, V. Staemmler, R. L. Vanderwal, *et al.*, J. Phys. Chem. **96**, 3201 (1992).
- ²S. A. Harich, D. W. H. Hwang, X. F. Yang, J. J. Lin, X. M. Yang, and R. N. Dixon, J. Chem. Phys. **113**, 10073 (2000).
- ³R. Schinke, V. Engel, and V. Staemmler, J. Chem. Phys. **83**, 4522 (1985).
- ⁴R. N. Dixon, Chem. Soc. Rev. **23**, 375 (1994).
- ⁵M. Brouard, S. R. Langford, and D. E. Manolopoulos, J. Chem. Phys. **101**, 7458 (1994).
- ⁶P. Andresen, V. Beushausen, D. Hausler, H. W. Lulf, and E. W. Rothe, J. Chem. Phys. **83**, 1429 (1985).
- ⁷R. L. Vanderwal, J. L. Scott, and F. F. Crim, J. Chem. Phys. **94**, 1859 (1991).
- ⁸R. Schinke, V. Engle, P. Andresen, D. Hausler, and G. G. Balintkurti, Phys. Rev. Lett. **55**, 1180 (1985).
- ⁹R. Schinke, R. L. Vanderwal, J. L. Scott, and F. F. Crim, J. Chem. Phys. **94**, 283 (1991).
- ¹⁰O. Votava, D. F. Plusquellic, and D. J. Nesbitt, J. Chem. Phys. **110**, 8564 (1999).
- ¹¹P. Andresen, G. S. Ondrey, B. Titze, and E. W. Rothe, J. Chem. Phys. **80**, 2548 (1984).
- ¹²G. G. Balintkurti, J. Chem. Phys. **84**, 4443 (1986).
- ¹³R. L. Vanderwal, J. L. Scott, F. F. Crim, K. Weide, and R. Schinke, J. Chem. Phys. **94**, 3548 (1991).
- ¹⁴M. Brouard and S. R. Langford, J. Chem. Phys. **106**, 6354 (1997); I. Bar, Y. Cohen, D. David, T. Arusiparpar, S. Rosenwaks, and J. J. Valentini, *ibid.* **95**, 3341 (1991); R. L. Vanderwal, J. L. Scott, and F. F. Crim, *ibid.* **92**, 803 (1990); D. F. Plusquellic, O. Votava, and D. J. Nesbitt, *ibid.* **109**, 6631 (1998).
- ¹⁵S. A. Nizkorodov, A. E. W. Knight, M. Ziemkiewicz, and D. J. Nesbitt (unpublished).
- ¹⁶D. F. Plusquellic, O. Votava, and D. J. Nesbitt, J. Chem. Phys. **107**, 6123 (1997).
- ¹⁷R. L. Vanderwal and F. F. Crim, J. Phys. Chem. **93**, 5331 (1989).
- ¹⁸C. A. Cantrell, A. Zimmer, and G. S. Tyndall, Geophys. Res. Lett. **24**, 2195 (1997).
- ¹⁹M. S. Child and L. Halonen, Adv. Chem. Phys. **57**, 1 (1984).
- ²⁰R. A. Toth, Appl. Opt. **33**, 4851 (1994).
- ²¹I. L. Chidsey and D. R. Crosley, J. Quant. Spectrosc. Radiat. Transf. **23**, 187 (1980).
- ²²D. Hausler, P. Andresen, and R. Schinke, J. Chem. Phys. **87**, 3949 (1987).
- ²³J. Z. Zhang and D. G. Imre, J. Chem. Phys. **90**, 1666 (1989).
- ²⁴K. Weide, S. Hennig, and R. Schinke, J. Chem. Phys. **91**, 7630 (1989).
- ²⁵K. S. Sorbie and J. N. Murrell, Mol. Phys. **29**, 1387 (1975).
- ²⁶V. Staemmler and A. Palma, Chem. Phys. **93**, 63 (1985).
- ²⁷R. T. Lawton and M. S. Child, Mol. Phys. **40**, 773 (1980).
- ²⁸R. J. Barnes, A. F. Gross, and A. Sinha, J. Chem. Phys. **106**, 1284 (1997).